

Inter-Laboratory Characterization of the Velocity Field in the FDA Blood Pump Model Using Particle Image Velocimetry (PIV)

PRASANNA HARIHARAN,¹ KENNETH I. AYCOCK,^{1,2} MARTIN BUESEN,³ STEVEN W. DAY,⁴ BRYAN C. GOOD,²
LUKE H. HERBERTSON,¹ ULRICH STEINSEIFER,³ KEEFE B. MANNING,² BRENT A. CRAVEN,¹
and RICHARD A. MALINAUSKAS¹

¹Food & Drug Administration, 10903 New Hampshire Avenue, Silver Spring, MD, USA; ²Pennsylvania State University, University Park, PA, USA; ³RWTH Aachen University, Aachen, Germany; and ⁴Rochester Institute of Technology, Rochester, NY, USA

(Received 2 July 2018; accepted 8 September 2018; published online 5 October 2018)

Associate Editors David A. Steinman, Francesco Migliavacca, and Ajit P. Yoganathan oversaw the review of this article.

Abstract

Purpose—A credible computational fluid dynamics (CFD) model can play a meaningful role in evaluating the safety and performance of medical devices. A key step towards establishing model credibility is to first validate CFD models with benchmark experimental datasets to minimize model-form errors before applying the credibility assessment process to more complex medical devices. However, validation studies to establish benchmark datasets can be cost prohibitive and difficult to perform. The goal of this initiative sponsored by the U.S. Food and Drug Administration is to generate validation data for a simplified centrifugal pump that mimics blood flow characteristics commonly observed in ventricular assist devices.

Methods—The centrifugal blood pump model was made from clear acrylic and included an impeller, with four equally spaced, straight blades, supported by mechanical bearings. Particle Image Velocimetry (PIV) measurements were performed at several locations throughout the pump by three independent laboratories. A standard protocol was developed for the experiments to ensure that the flow conditions were comparable and to minimize systematic errors during PIV image acquisition and processing. Velocity fields were extracted at the pump entrance, blade passage area, back gap region, and at the outlet diffuser regions. A Newtonian blood analog fluid composed of sodium iodide, glycerin, and water was used as the working fluid. Velocity measurements were made for six different pump flow conditions, with the blood-equivalent flow rate ranging between 2.5 and 7 L/min for pump speeds of 2500 and 3500 rpm.

Results—Mean intra- and inter-laboratory variabilities in velocity were ~10% at the majority of the measurement locations inside the pump. However, the inter-laboratory variability increased to more than ~30% in the exit diffuser region. The variability between the three laboratories for the peak velocity magnitude in the diffuser region ranged from 5

to 25%. The bulk velocity field near the impeller changed proportionally with the rotational speed but was relatively unaffected by the pump flow rate. In contrast, flow in the exit diffuser region was sensitive to both the flow rate and the rotational speed. Specifically, at 3500 rpm, the exit jet tilted toward the inner wall of the diffuser at a flow rate of 2.5 L/min, but the jet tilted towards the outer wall when the flow rate was 7 L/min.

Conclusions—Inter-laboratory experimental mean velocity data (and the corresponding variance) were obtained for the FDA pump model and are available for download at https://ncipub.org/wiki/FDA_CFD. Experimental datasets from the inter-laboratory characterization of benchmark flow models, including the blood pump model presented herein and our previous nozzle model, can be used for validating future CFD studies and to collaboratively develop guidelines on best practices for verification, validation, uncertainty quantification, and credibility assessment of CFD simulations in the evaluation of medical devices (e.g. ASME V&V 40 standards working group).

Keywords—Particle image velocimetry, PIV, Benchmark model, CFD validation, VVUQ, Computational fluid dynamics, FDA.

INTRODUCTION

Computational fluid dynamics (CFD) is an important tool used for designing and predicting the performance of a variety of medical devices. In recent years, CFD modeling has been increasingly used in making safety and effectiveness claims as part of medical device submissions for devices seeking marketing clearance from the U.S. Food and Drug Administration (FDA).¹⁷ CFD data have been used as a part of regulatory submissions for cardiovascular

Address correspondence to Prasanna Hariharan, Food & Drug Administration, 10903 New Hampshire Avenue, Silver Spring, MD, USA. Electronic mail: Prasanna.Hariharan@fda.hhs.gov

and renal devices such as blood pumps, ventricular assist devices (VADs), heart valves, catheters, hemodialyzers, oxygenators, stents, and endovascular grafts. CFD is used primarily as a pre-market evaluative tool to support 510(k) Pre-market Notifications, Investigational Device Exemption (IDE), and Pre-Market Approval (PMA) submissions. However, some post-market studies involving root-cause analyses to understand device failures have also used CFD as an assessment tool. While the use of CFD in regulatory submissions is increasing, and expanding to new areas such as neurological devices, the role of CFD in the regulatory decision-making process remains limited. However, numerous initiatives are under way to expand the use of CFD in medical device regulatory submissions, and CFD modeling continues to be a top regulatory science priority for FDA.^{4,17}

The main reason for the limited model influence on decision making is a lack of credibility in the CFD data provided in regulatory submissions. This lack of credibility stems from a variety of reasons that includes inadequate verification and validation, and a disconnect between the validation conditions and the real context of use of the medical device. To address these issues and others, the FDA, academia, industry, and software developers have been involved in several collaborative activities for enhancing the credibility of CFD models used in device design, testing, and in regulatory submissions.^{9,11,28,30} For instance, FDA and industry are collaborating on the development of a risk-informed credibility assessment framework through the ASME V&V 40 Subcommittee, which is devoted to verification and validation of computational modeling applied to medical devices.²⁸ FDA also recently released a guidance document that provides details about how to report computational modeling studies as part of regulatory submissions.³⁰

Development of benchmark geometries and validation datasets enhances the accuracy and credibility of CFD models within the field; standardized geometries and datasets are widely used by other industries, particularly in the aerospace and energy sectors.^{14,16,19,32} To validate computational data for complex systems, Oberkampf *et al.*²⁰ recommends a hierarchical approach starting with verifying and validating the codes using simple and generic benchmark cases, before applying the model to more complex sub-systems. The advantage of benchmark cases is that high-quality, reproducible experimental results can be obtained without involving multi-physics interactions, such as coupled fluid-flow/heat transfer or fluid-flow/structural mechanics interactions that are commonly assessed through complex device-level simulations.

Similar to the aerospace and energy sectors, government agencies and research groups are sponsoring and conducting round-robin (i.e., inter-laboratory)

studies to evaluate the ability of commercial and open-source CFD codes to accurately simulate fluid flow in various benchmark medical devices and physiological geometries.^{10,15,24,31} Steinman *et al.*²⁴ obtained pressure measurements across a standard aneurysm geometry and compared the empirical results with round-robin CFD predictions from 25 different participants.²⁴ The pressure drop predictions made by the CFD modelers matched within 8% with each other. However, large variabilities between the CFD results were noticed for predicting local aneurysm flow patterns. Similarly, the FDA developed a benchmark nozzle flow model that caused flow patterns representative of those occurring in devices such as catheters, hemodialysis tubing sets, cannulae, and syringes. *In vitro* measurements of velocity, shear stress, pressure, and hemolysis were acquired in three independent laboratories to establish ranges of measurement error and to account for laboratory-specific biases. The experimental data were then compared with round-robin CFD data provided by participants from 29 different groups.²⁶ An analysis of round-robin CFD velocity data revealed significant variability between simulations and the experiments. Similarly, the accuracy of the CFD results showed no correlation with the user's CFD experience, and the types of software and solver used by the participants. Further, the results showed the need for improving models of transitional flow as many medical devices operate in this flow regime.

Details on the benchmark models, the CFD simulation challenges, and the experimental results can be found at https://nciphub.org/wiki/FDA_CFD. The nozzle benchmark geometry and the corresponding validation data are increasingly being used by modelers to validate and improve in-house, open-source, and commercial CFD solvers.^{3,6,7,12,13,21,23,27,33,34} The nozzle validation data have been used for evaluating the accuracy of large eddy simulation (LES) models,^{3,6,13,34} the Lattice Boltzmann method for laminar flows,³³ direct numerical simulation (DNS) solvers,²¹ and traditional Reynolds Averaged Navier–Stokes (RANS) turbulence models.^{7,27}

As a continuation of the same effort, an FDA-coordinated research team²⁶ developed a generic centrifugal blood pump with a simple rotor and housing geometry as a second benchmark model. The centrifugal pump was employed because CFD is often used in the design and evaluation of circulatory assist devices. Like the nozzle model, measurements of velocity, pressure, and shear stress were acquired by three independent laboratories. To minimize user errors and laboratory biases, a standard protocol for performing the Particle Image Velocimetry (PIV) measurements was collaboratively developed for this

study. Flow data were collected at specific cross-sections to effectively capture the different flow phenomena occurring in the pump. *In vitro* hemolysis levels caused by the pump over a range of operating conditions were obtained in one testing lab. Participants from 25 different groups performed CFD simulations using the pump. Each group predicted the flow, with a subset of that group providing hemolysis data to FDA for analysis.¹⁵

The primary goal of this article is to present the experimental protocol and the inter-laboratory pressure and velocity data obtained from the PIV measurements of the FDA blood pump in three separate laboratories. Noteworthy aspects of this dataset include characterizing lab-to-lab variability and identifying flow features indicative of pump performance and blood damage potential (e.g. areas of low flow and recirculation). The applicability of the inter-laboratory PIV results for validating the round-robin CFD data is assessed in the discussion section. The benchmark data are available to the scientific community through an online repository for use in future CFD validation studies (https://nciphub.org/wiki/FDA_CFD).

METHODS

Centrifugal Blood Pump

To aid in PIV visualization, the primary components of the centrifugal blood pump (i.e., front and rear housings, impeller, blades, outlet volute) were machined out of transparent acrylic.^{8,15} The main opaque components included the impeller shaft and the threaded hub connecting the acrylic impeller to the shaft, which were both made out of stainless steel. The

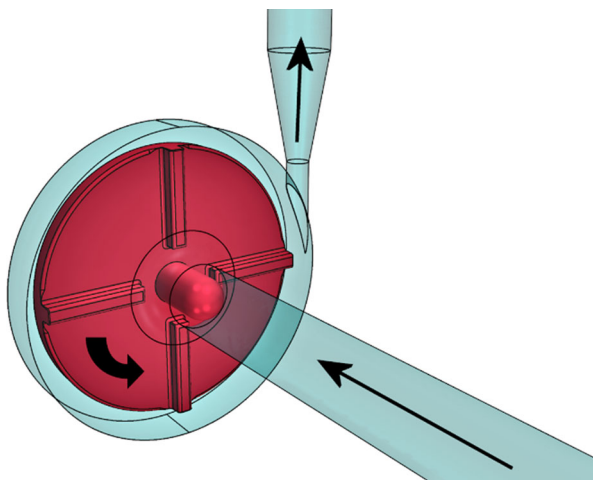


FIGURE 1. The FDA blood pump: an idealized centrifugal pump with four straight blades equally spaced around a circular impeller.

blood pump was designed to have simple geometrical features and a broad operating range (Fig. 1). The 3D computer-aided design file of the pump geometry is available for download at https://nciphub.org/wiki/FDA_CFD/ComputationalRoundRobin2Pump. The pump rotor had a diameter of 52 mm with four blades situated at 90° angles to one another. Each impeller blade was 3 mm wide, 3 mm tall, and 18.5 mm long (Fig. 2). The rotor edges were filleted, with radii ranging from 0.17 mm at the blade top edge to 0.6 mm along the long edges of the blade. The clearances between the front housing and blade top, and between the back housing and back rotor face, were set to 1 mm.

The inner diameter of the pump housing chamber was 60 mm. The clearance between the housing and the outer rotor rim was 4 mm. The acrylic model housing used for experiments had a minimum measured fillet radius of 0.04 mm at the cutwater.

Pump components fabricated out of extruded transparent acrylic were hand-polished to improve the optical properties and to meet quality control tolerance levels. Individual pumps including components such as motor, shaft, impeller, front and back housings were made for each laboratory. Quality control measurements ensured that the physical dimensions of the pumps were within 1% of the design specifications and surface finishes were $R_a < 0.6 \mu\text{m}$ ($R_a = 0.24 \pm 0.23 \mu\text{m}$, Contour GT-K 3D Optical Microscope, Bruker AXS, Madison, WI) for all fluid-contacting pump components.

Flow Loop

A schematic of the testing flow loop is shown in Fig. 3. The flow loop contained a modified 500 ml blood bag reservoir fitted with a custom resin bottom piece containing inlet and outlet ports (Fig. 3) to improve mixing inside the reservoir and to avoid particle accumulation by minimizing low-flow regions. An ultrasound flow probe (Transonic systems, Ithaca, NY) was utilized to measure the fluid flow rate, which ranged from 2.5 to 7.0 L/min. An adjustable tubing clamp was used to control the flow rate and back pressure of the pump.

An acrylic tube guide was designed and installed to maintain a constant radius of curvature of 9 cm for the inlet tubing line (Fig. 3). The 12 mm diameter inlet tube was curved to allow for placement of the PIV camera in front of the pump. An inline heat exchanger with a circulating water bath helped to maintain the temperature of the blood-analog fluid at a constant desired value which ranged between 23 and 27 °C depending upon the laboratory. Identical tubing, with

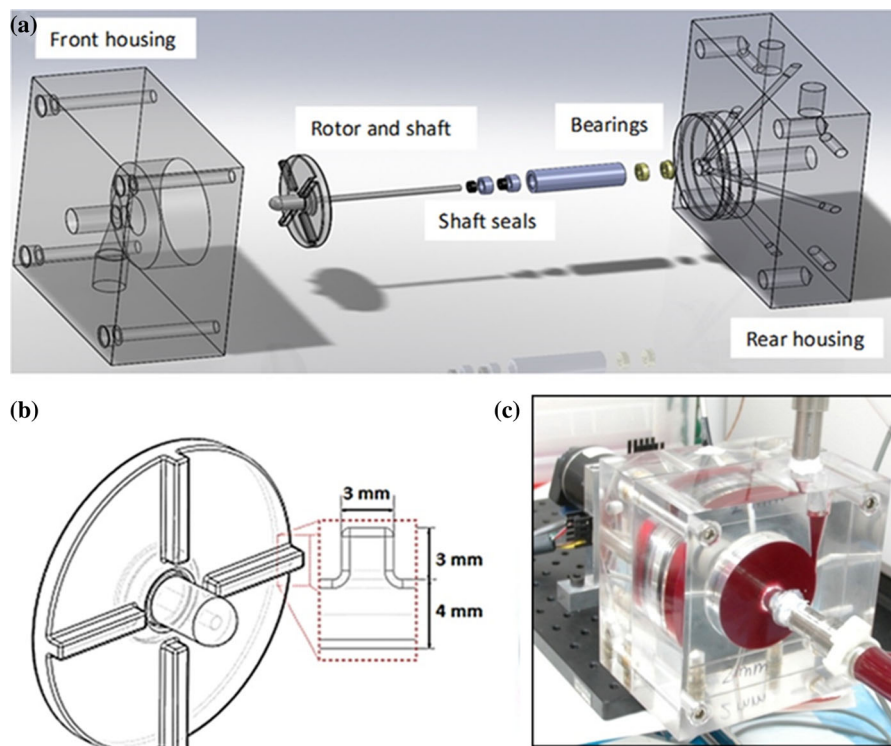


FIGURE 2. Images of the: (a) pump assembly, (b) impeller blade dimensions, and (c) physical model of the pump tested with animal blood.

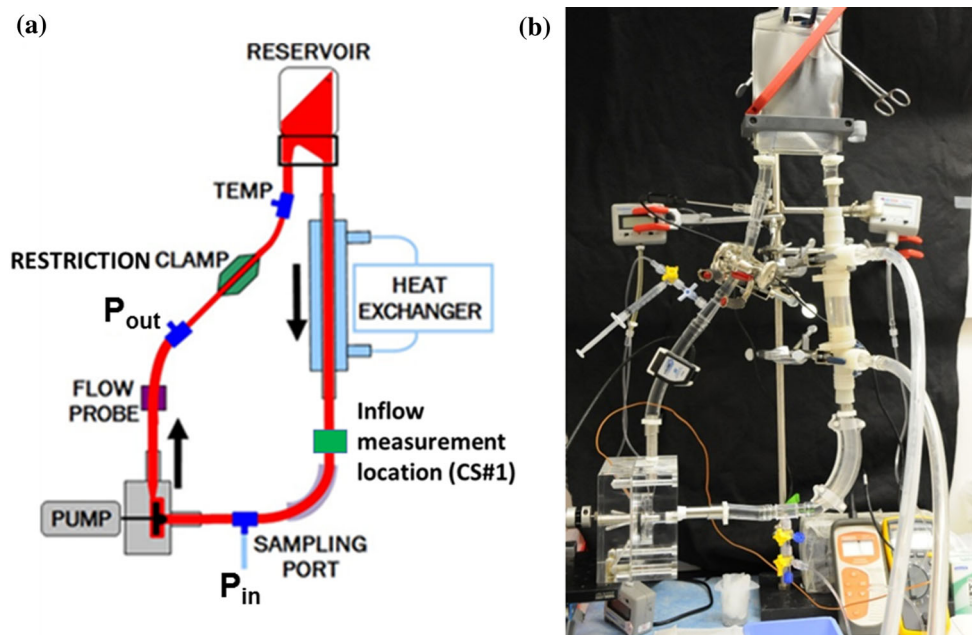


FIGURE 3. (a) Schematic and (b) photograph of the pump testing flow loop.

specified diameters and lengths, and identical tubing connectors were used across all three PIV laboratories.¹⁵ Two pressure probes (Model 200-2000IN, Netech, Inc., Farmingdale, NY, USA) were utilized to

measure the pressure head across the pump. A temperature probe was connected to the loop for monitoring temperature (Temp 5 Acorn series, Source: Cole-Parmer, Vernon Hills, IL, USA).

TABLE 1. Fluid properties for the PIV experiments.

Lab	Viscometer	Dynamic viscosity (cP)	Specific gravity	Kinematic viscosity (cSt)	Refractive index
Lab-1	AMv (Anton Paar, Vienna, Austria)	6.2	1.74	3.57	1.485
Lab-2	Vilastic (Vilastic Scientific Inc., Austin, TX)	6	1.68	3.56	1.485
Lab-3	DV-III (Brookfield Engineering Laboratories, Inc., Middleboro, MA)	5.2–6.5	1.6–1.75	3.3–3.7	1.486

Shear rates at which the viscosities were measured ranged between 100 and 250 1/s.

TABLE 2. Flow conditions for blood damage, CFD, and PIV studies (assuming blood dynamic viscosity = 3.5 cP and density = 1035 kg/m³).

Condition #	Conditions for blood damage experiments and CFD simulations		Normalized values				Example operating conditions for PIV experiments	
	Flow rate (L/min)	Pump Speed (rpm)	Reynolds number in the pump (Re)	Reynolds number (CS#1)	Flow coefficient (ϕ)	Turbulence intensity at CS #1 (%)	Flow rate (L/min)	Pump speed (rpm)
1	2.5	2500	209,338	1307	0.00113	4	2.64	2640
2	2.5	3500	293,073	1307	0.00081	4	2.64	3696
3	4.5	3500	293,073	2353	0.00146	5	4.75	3696
4	6.0	2500	209,338	3137	0.00272	7	6.34	2640
5	6.0	3500	293,073	3137	0.00194	7	6.34	3696
6	7.0	3500	293,073	3660	0.00226	7	7.39	3696

The table also presents a representative set of flow conditions for PIV experiments with the blood analog fluid with viscosity and density of 6.0 cP and 1680 kg/m³, respectively. CS#1 represents cross-section #1 at the pump inlet as described in the text.

Blood Analog Fluid

Although blood behaves as a non-Newtonian, viscoelastic and shear thinning fluid at relatively low shear rates (< 100 1/s,¹), at higher shear rates it reaches an asymptotic viscosity and its rheological behavior becomes approximately Newtonian. Given the relatively high shear rates encountered in continuous-flow centrifugal blood pumps, a Newtonian fluid is commonly used in experimental and computational studies of these devices.² The Newtonian approximation was applied herein to simplify fluid preparation and to facilitate similarity scaling for comparison to the blood experiments. The Newtonian blood analog was composed of approximately 50% sodium iodide (NaI), 17% glycerin, and 33% water, by weight. The dynamic viscosity of the fluid ranged between 5.2–6.5 cP and the fluid density ranged from 1600 to 1750 kg/m³ among the laboratories due to differences in fluid preparation and operating temperature (Table 1). The refractive index of the blood analog fluid, which was measured using a digital handheld refractometer (PA202, Palm Abbe, Cleveland, OH) in each lab, was less variable and ranged between 1.48 to 1.49.

Although the fluid composition and operating temperature varied among the labs, the critical non-

dimensional parameters (i.e., the pump Reynolds number and the flow coefficient) were maintained the same across the labs for all 6 test conditions to ensure consistency (Table 2). The results were then dimensionalized using a representative blood viscosity of 3.5e-3 Pa.s and density of 1035 kg/m³ (i.e., the same properties used in the round-robin CFD simulations).

Details on the particles used for the PIV measurements are provided in Table 3. Fluorescent particles were used as tracer particles by two of the three laboratories. The use of fluorescent particles improved the accuracy of near-wall velocity and shear stress measurements by filtering the incident laser light reaching the camera. The excitation and emission wavelengths for these particles are 532 and 610 nm, respectively.

The blood pump was mounted on a stage that enabled movement in three directional planes. The position of the laser sheet and the camera were fixed after calibrating the PIV image at select cross-sections. A digital laser tachometer was used to measure the pump rotational speed.

Since the corresponding round-robin CFD simulations and blood damage experiments were carried out using nominal blood properties (dynamic viscosity = 3.5 cP and density = 1.035 g/cc), all flow

TABLE 3. Standard protocol for PIV experiments.

Experimental parameter	Lab-1	Lab-2	Lab-3
Temperature control	Inline heat exchanger	Inline heat exchanger	Inline heat exchanger
Flow loop temperature (°C)	30	23	25
Temperature fluctuations (°C)	± 1	± 0.4	± 0.5
Flow rate and rpm fluctuations (%)	< 1	< 1	< 1
Conversion factor—used to obtain the pump rotational speed and flow rate for each runs, and to convert PIV velocity to blood equivalent values assuming the blood viscosity of 3.5 cP and density of 1050 kg/m ³	1.05	1.06	0.95 – 1.05
Tracer particle	Monodisperse Rhodamine B-labeled highly crosslinked melamine resin particles (MF-RhB polymer particles); Distributor: microParticles GmbH, Germany	Spherglass 5000 Solid Glass Microspheres, Potter Industries Inc., Valley Forge, PA	Fluorescent polyamide spheres (Fluoro-Max 36-3B; Thermo Scientific Inc., Fremont CA)
Particle size (microns)	10	10	8–10
Particle image size (pixels)—obtained from PIV images	~ 2	~ 2	~ 2
Particle seeding density (number of particles/interrogation window)	> 10	> 10	> 10
Laser	Nd-YAG	Nd-YAG	Nd-YAG
Laser transmission	Laser-head → articulating arm → cylindrical lens	Laser-head → articulating arm → cylindrical lens	Laser-head → cylindrical lens
Laser sheet thickness	0.8 mm (burn paper method)	0.5 mm (burn paper method)	0.6 mm (scanning pin-hole profiler method)
PIV camera	MK III (Dantec Dynamics) CMOS Chip	TSI PIVCAM 14-10	LaVision Imager Pro X
Pixel resolution (of the camera) (microns)	9–11	11	11
Interrogation window size (pixels)	32 axially × 16 radially (50% overlap)	32 × 32	32 × 32 (50% overlap)
Mesh size (i.e., distance between the PIV vectors)	CS#2,3,4 = 0.55 mm CS#5 = 0.28 mm	0.25 mm	CS#2,3,4 = 0.48 mm CS#5 = 0.33 mm
Number of image pairs	500	500	500–2500
PIV software used	Dynamic Studio 2.3 (Dantec Dynamics)	INSIGHT 3G, TSI, Inc., Shoreview, MN	DAVIS FLOWMASTER 8.6, LaVision Inc., Ypsilanti, MI
PIV pre-processing of images	None	None	None
PIV algorithm	Dynamic Studio Algorithm, Adaptive Correlation, with moving average filter (acceptance factor = 0.1)	Multi-pass cross-correlation with a 'Recursive Nyquist Grid' method, initial and final window sizes of 64 × 64 and 32 × 32 pixels, 'Hart Correlator' with a 'Bilinear Peak' correlation engine	Multi-pass cross-correlation algorithm with initial and final window sizes of 64 × 64 and 32 × 32 pixels

quantities for the PIV experiments were scaled to match the CFD conditions using the Reynolds number and the flow coefficient.

$$\text{Reynolds number (Re)} = \frac{\rho n D^2}{\mu} \quad (1)$$

$$\text{Flow coefficient } \varphi = \frac{Q}{n D^3} \quad (2)$$

where ρ is the density, n is the pump rotational speed, μ is the dynamic viscosity, D is the impeller diameter (5.2 cm), and Q is the fluid flow rate.

Flow conditions

Six different flow conditions with flow rates ranging from 2.5 to 7 L/min and pump rotational speeds ranging from 2500 rpm to 3500 rpm were evaluated in this study (Table 2). To aid in inter-laboratory comparison of the PIV data and for comparison with the round-robin CFD study, the pump Reynolds number and the flow coefficient were maintained the same across the laboratories. Depending upon the fluid viscosity and density (which were measured before the start of the experiments on each day), the pump rota-

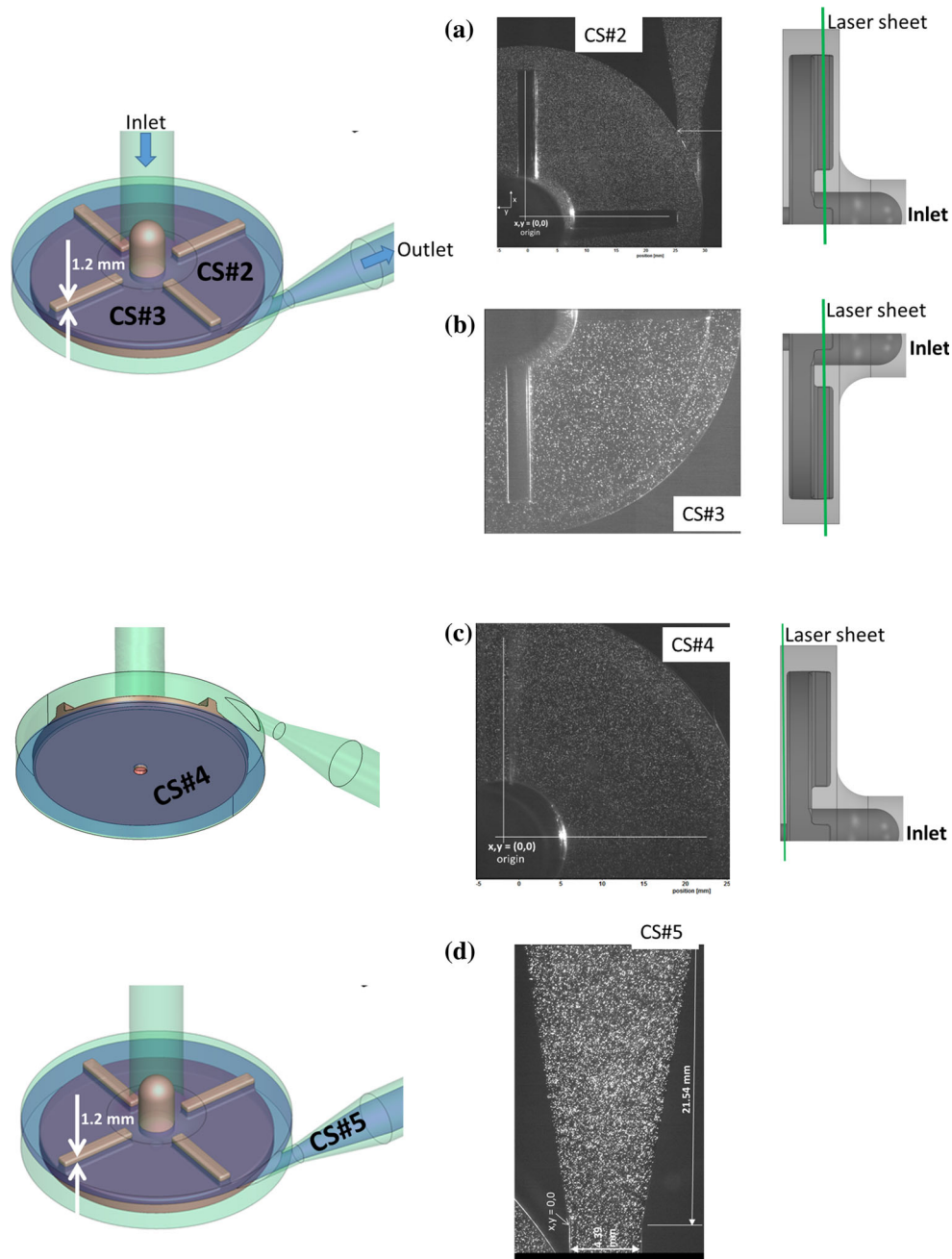


FIGURE 4. Measurement planes inside the pump and sample PIV images: (a) blade passage region (CS#2 in upper quadrant 1), (b) Blade passage region (CS#3 in lower quadrant 2), (c) back-gap region beneath upper quadrant 1, and (d) diffuser region (i.e., CS#5 the pump outlet diffuser). Location of CS#1 is shown in Fig. 3a.

tional speed and flow rate were adjusted to maintain the same pump Re and ϕ values for each test condition. Table 2 includes a representative set of flow conditions for PIV experiments with the blood analog fluid with viscosity and density of 6 cP and 1680 kg/m³, respectively. Previous studies have discussed different blood analog fluids that can match the index of refraction of the acrylic.^{5,18} While the density of our blood analog fluid is higher than blood (1650 vs.

1035 kg/m³), the dynamic viscosity is also higher by the same factor (5.2–6.5 vs. 3.5 cp). As a result, the kinematic viscosity of our fluid is very similar to that of blood used in the round-robin CFD simulations (3.3–3.7 vs. 3.4 cSt). Consequently, the conversion factor was close to 1 (0.96–1.06) while using our blood analog solution. Turbulent intensity at the inlet was estimated by measuring the mean and RMS components of velocity obtained from multiple PIV image pairs (Ta-

ble 3) for each test condition. The pressures at the pump inlet and exit were also measured for comparison to the blood experiments and the CFD simulations.

Measurement Planes

PIV measurements were made at 12 different cross-sections (CS) covering different regions of the pump. A total of four PIV and pressure measurement datasets were obtained from the three labs, as one lab (Lab-3) provided two separate datasets. Lab-3 obtained two separate data-sets to measure intra-laboratory variability in the velocity data. The two datasets were obtained using the same pump but at different times (separated by 6 months). To ensure the runs were independent, the pump and the flow loop components were dismantled and reassembled again, and a separate batch of test fluid was used for each set of experiments. In addition to acquiring another dataset, Lab-3 also obtained data in additional cross-sections. (19 different cross-sections compared to 12 cross-sections for the other two labs). PIV data for a subset of the cross-sections are presented in this study as they contain several inter-related flow features which characterize the performance of the pump. The five PIV-analyzed CS regions are as follows:

- (i) Inflow region (CS#1): A separate acrylic extension block (green shaded region in Fig. 3a) was placed before the loop curvature to obtain the inflow velocity profile upstream of the pump.
- (ii) Blade passage region (CS#2 and 3): For these cross-sections, the laser sheet passed through

a plane located within the blade passage region, 1.2 mm from the top of the impeller blades (Fig. 4a and 4b). PIV data from two different quadrants of the impeller were analyzed in this study.

- (iii) Back-gap region (CS#4) : To measure the flow beneath the rotor, the laser sheet was passed through a plane located 0.5 mm from the back of the impeller (Fig. 4c). The total thickness of the back-gap region was 1 mm.
- (iv) Outlet diffuser region (CS#5): PIV data were obtained in a cross-section at the exit diffuser region of the pump (Fig. 4d).

More information about precise locations of these cross-sections and additional ones not presented in this study can be obtained from https://nciphub.org/wiki/FDA_CFD/ComputationalRoundRobin2Pump.

PIV measurements

The PIV images were captured *via* a charge coupled device (CCD) or a complementary metal–oxide–semiconductor (CMOS) camera. The visualized blade position in the PIV images was frozen to the same location by synchronizing the laser pulse trigger with impeller orientation. The phase-averaged two-dimensional velocity field was obtained by averaging the cross-correlation results of 500–2500 pairs of images captured with one of the blades positioned 90° to the pump outlet diffuser. Commercially available multi-pass cross-correlation algorithms (DAVIS FLOW-MASTER, LaVision Inc., Ypsilanti, MI, Dynamic Studio, and INSIGHT 3G, TSI, Inc., Shoreview, MN) were used for processing the particle images. The particle image size and the seeding density were ~ 2 and > 10, respectively. The final spatial resolution of the PIV velocity measurements depended on the required field of view in the sampling cross-sections. For example, a coarse resolution of 0.4–0.6 mm was used to capture images of an entire pump quadrant to measure the velocity field between the rotating blades (e.g. CS#2) for Lab #1 and 3, whereas the PIV resolution was 0.28–0.33 mm for the exit diffuser region in CS#5. The best practice procedures for performing PIV, which were established during the nozzle study, were followed for analyzing the pump data.¹⁰

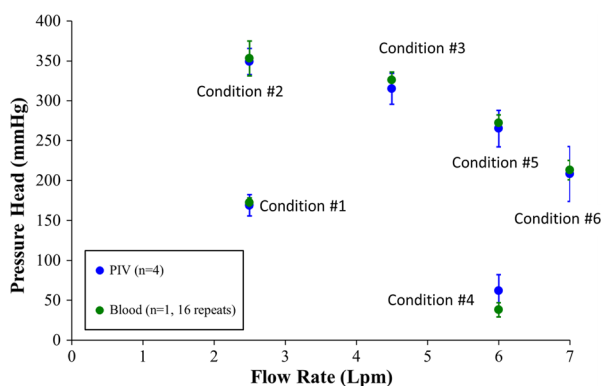


FIGURE 5. Pressure–flow curves for the PIV and blood damage experiments. Values were measured using the blood analog fluid during the PIV experiments compared with values obtained using porcine blood during hemolysis testing. The pump affinity laws (Eqs. 1–2) were used to scale the flow rate values to the corresponding CFD simulation and hemolysis testing conditions. Conditions #1 and #4 were at a pump speed of 2500 rpm, all other conditions at 3500 rpm.

RESULTS

Unless stated otherwise, the inter-laboratory variabilities in pressure and velocity are expressed in terms of the Coefficient of Variation (CoV), which is estimated as standard deviation (1σ)/local mean*100%.

Pressure–Flow curve

Measurements of the pressure rise (from pump inlet to outlet) from the three PIV labs agreed within $\sim 10\%$ for conditions #1, 2, 3, and 5, but variability was greater for condition #6 at 32% (Fig. 5). Except for condition #4, the mean pressure measured during the PIV experiments matched the pressure data from hemolysis testing to within $\sim 5\%$ (Fig. 5). During PIV measurements, a maximum pressure rise of 349 ± 16 mmHg was measured for condition #2 (3500 rpm and 2.5 L/min) and a minimum rise of 62 ± 20 mmHg was measured for condition #4 (2500 rpm and 6 L/min). The inter-laboratory variability was the highest for condition #4 at $\sim 33\%$.

Inflow Velocity Profile (CS#1)

Flow in the 12 mm diameter inflow tubing was laminar ($Re = 1307$) for the lowest flow rate of 2.5 L/min, although it was not fully developed as evidenced by the blunt flow profile (Fig. 6). The flow became turbulent at the higher flow rates, with turbulence intensities (TI) increasing to a maximum of 7% at the peak flow rate of 7 L/min (Table 2). The upstream inflow velocity profile data and the mean TI values were provided to the CFD modelers during the round-robin study to guide the specification of inlet flow boundary conditions in the computational simulations.

Blade Passage Region (CS#2,3)

The inter-laboratory mean velocity field and the corresponding coefficient of variation (CoV) for CS#2 are provided for conditions #1–6 (Figs. 7 and 8). For all conditions at this cross-section, the mean CoV for velocity magnitude was $\sim 10\%$ (Fig. 8). The corre-

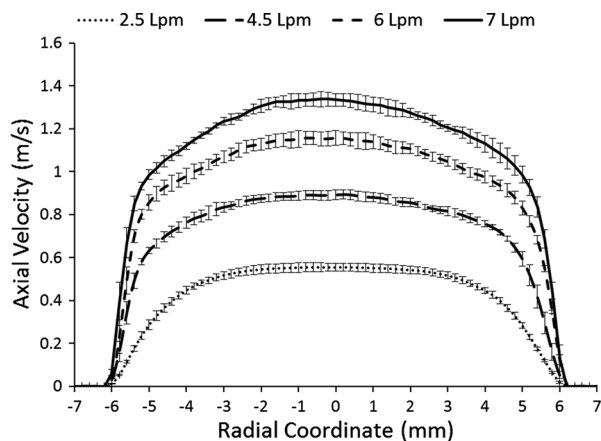


FIGURE 6. Mean axial velocity profile measured at the entrance to the curved inflow tube upstream of the pump for all the flow rates considered in this study.

sponding intra-laboratory variabilities for the two Lab-3 datasets were similar with the CoVs less than 10%. However, the local CoV values were as high as 20% near the vertical blade and the rotor hub region (Fig. 8). Figure 7b also shows the RMS velocity normalized to the local mean velocity for individual laboratories. In general, Lab-2 had the greatest RMS velocity (2–3 times more) compared to the other two PIV laboratories.

For each condition, the velocity magnitude inside the pump increased along the outward radial direction (Figs. 7 and 8). Peak velocity magnitudes were on the order of 10% lower than the corresponding blade velocity, calculated as ωr [where $\omega = 2\pi n/60$, n is the pump speed (2500 or 3500 rpm), and r is the radius along the blade (25.4 mm)] (Figs. 7 and 8). The peak velocity was measured not at the blade tip (26 mm) but 0.6 mm below the tip of the blade.

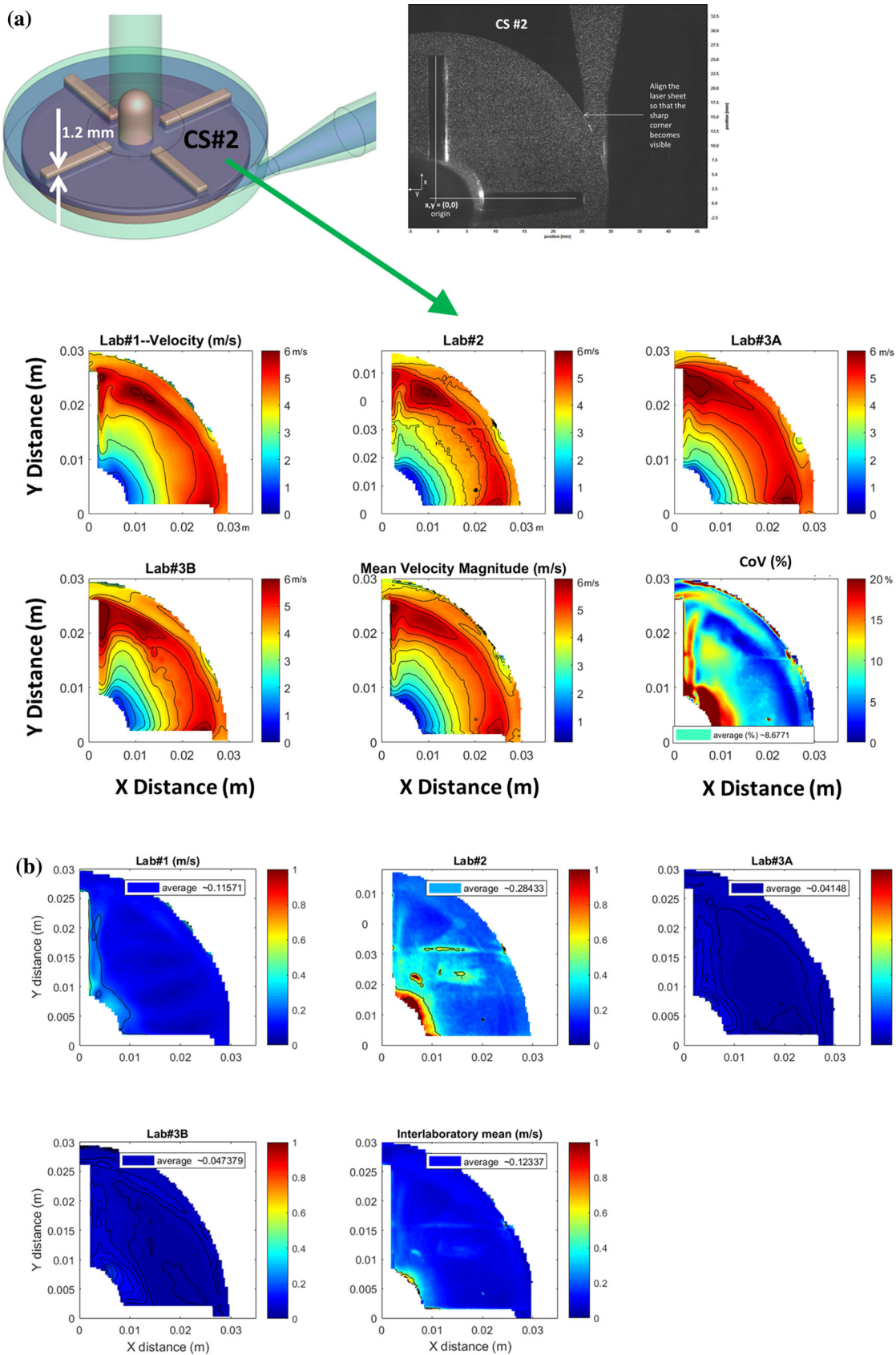
Despite the difference in flow rate among the conditions (ranging from 2.5 to 7 L/min), the velocity contours were qualitatively similar (Fig. 8). The flow was dominated by the tangential component of velocity except near the vertical blades and the outlet diffuser, where the radial velocity component was prominent (Fig. 8). The radial velocity component increased with flow rate while the tangential component scaled with pump rotational speed (Fig. 8).

Radial velocity profiles extracted along the diagonal bisecting CS#2 show that, for the same rotational speed, the radial distribution of flow changed depending upon the flow rate (Fig. 9a). Specifically, as the flow rate increased from 2.5 to 6 L/min, the location of the peak velocity shifted outward by ~ 1 mm for both rotational speeds (Fig. 9a). Furthermore, for $r < 26$ mm, the velocity magnitudes for the lower flow rate (condition #1 and 2) were greater than for a higher flow rate (conditions #4 and 5), respectively, while for $r > 26$ mm the opposite is true (Fig. 9a).

Differences in the velocity profiles at the same rotational speed (e.g. condition #1, 2500 rpm, 2.5 L/min) but at different flow rates (e.g. condition #4, 2500 rpm, 6 L/min) were less pronounced in the second quadrant, which is located upstream of the diffuser region (Fig. 9b).

Back-Gap Region (CS#4)

For this location, the optical images from one of the laboratories (Lab-2) contained artifacts from excessive laser light scattering by the impeller disc and the blades that rendered the PIV images with too much artifact to use. Hence, the mean velocity and CoV for this location were obtained excluding the data from Lab-2. Similar to the other cross-sections, the inter-laboratory



◀ **FIGURE 7.** (a) Example of velocity magnitude contours from each PIV laboratory in the blade passage region (CS#2) for flow condition #1 (2500 rpm, 2.5 L/min). Lab-3 provided two separate data sets (3A and 3B). The center of the rotor hub is at coordinates (0, 0). (b) Example of RMS velocity normalized with local velocity from each laboratory in the blade passage region (CS#2) for flow condition #1 (2500 rpm, 2.5 L/min). The spatially averaged normalized RMS velocity is highlighted.

variability (i.e., CoV) was around 10% and comparable to the intra-laboratory variability ($\sim 7\%$).

Velocity magnitude in the 1-mm gap region beneath the rotor increased linearly with the impeller radius until $r = 25$ mm (Fig. 10). For $r > 25$ mm, the velocity increased considerably, with the peak occurring near the outer edge of the rotor (Fig. 10). The velocity magnitude was proportional to the impeller rotational speed. For example, maximum velocity magnitudes of 3.9 and 5.5 m/s occurred near the outer edge of the impeller for pump speeds of 2500 and 3500 rpm, respectively.

Similar to the blade passage region, there were some differences in the radial flow profiles for the different flow rates (Fig. 11). Specifically, the velocity magnitude for the 2.5 L/min cases was higher than for the 6 L/min cases for $r < 28$ mm (Fig. 11).

Outlet Diffuser Region (CS#5)

Peak velocity in the diffuser region was proportional to the flow rate, with maximum velocities of 4.0 ± 0.2 and 8.4 ± 0.7 m/s measured for the 2.5 L/min (condition #2) and 7 L/min (condition #6) scenarios, respectively (Fig. 12a). The direction of the exit jet was dependent upon both the flow rate and the pump rotational speed. Jet direction was determined based on the in-plane jet center-line, obtained by extracting the location of peak velocity for each Y location along the length of the diffuser (Fig. 12b). Except for conditions #1 and 3 (2500 rpm and 2.5 L/min, 3500 rpm and 4.5 L/min), the jet was asymmetric and tilted either away from or towards the pump housing depending upon the flow rate (Fig. 12b). For condition #2 (i.e., highest rotational speed and lowest flow rate), the exit jet followed the direction of rotation and was attached to the inner wall of the diffuser, creating a large recirculation region on the outer wall (Fig. 12a). For condition #6 (i.e., highest flow rate), the jet was instead tilted towards the outer wall of the diffuser creating a recirculation region on the opposite side (Fig. 12a).

The variability between the three laboratories for the peak velocity magnitude in the diffuser region ranged from 5–25% (Fig. 13). While the level of asymmetry differed between labs (Fig. 13), the jet direction was consistent for all six flow conditions

(data not shown). However, flow profile shapes showed increasing inter-laboratory variability moving downstream in the diffuser (Fig. 13). Indeed, the coefficient of variation for velocity was highest in this cross-section (CS#5), with mean inter-laboratory CoV values exceeding 35%. In comparison, the CoVs for velocities inside the pump were typically less than $\sim 10\%$. The intra-laboratory variability was also high ($\sim 17\%$) in this region compared to the data obtained inside the pump ($\sim 10\%$). The fluctuations in the velocity field (represented by error bars in Fig. 13) increased downstream along the exit diffuser. Unlike the blade passage region (Fig. 7b), the magnitude of velocity fluctuations are similar among all three laboratories.

DISCUSSION

As part of an effort by the FDA to improve the credibility of CFD in the evaluation of medical devices, this inter-laboratory study was performed to obtain a benchmark validation dataset for a simplified blood pump model. The velocity and pressure data presented in this study, as well as velocity components for additional pump locations, are available on-line for download at https://nciphub.org/wiki/FDA_CFD. Similar to our previous nozzle model fluid dynamic dataset, the experimental data from the blood pump can be used for validating and providing better understanding of new and existing CFD codes, especially for predicting flow through centrifugal blood pumps.^{3,6,7,13,23} Previous CFD round-robins utilizing the FDA nozzle and aneurysm geometries showed that the CFD codes were capable of predicting the pressure data reasonably well. However, several of the CFD simulations of these models showed difficulty in accurately predicting the local velocity fields. Consequently, the inter-laboratory velocity data obtained from these benchmark geometries will be a meaningful resource and can be used by CFD modelers to improve and validate the accuracy of their CFD codes.

However, validating CFD simulations with the FDA nozzle and blood pump does not ensure that the CFD model is credible enough to make safety and performance predictions in real and more complex medical devices. The applicability of the validation data presented herein to other centrifugal blood pumps depends upon several factors, including similarities in geometrical features and flow characteristics between the devices, the context of use of the CFD model, and the intended use of the device. Despite this limitation, validation of CFD simulation models with benchmark experimental cases can be a helpful first-step towards estimating model-form error and establishing the

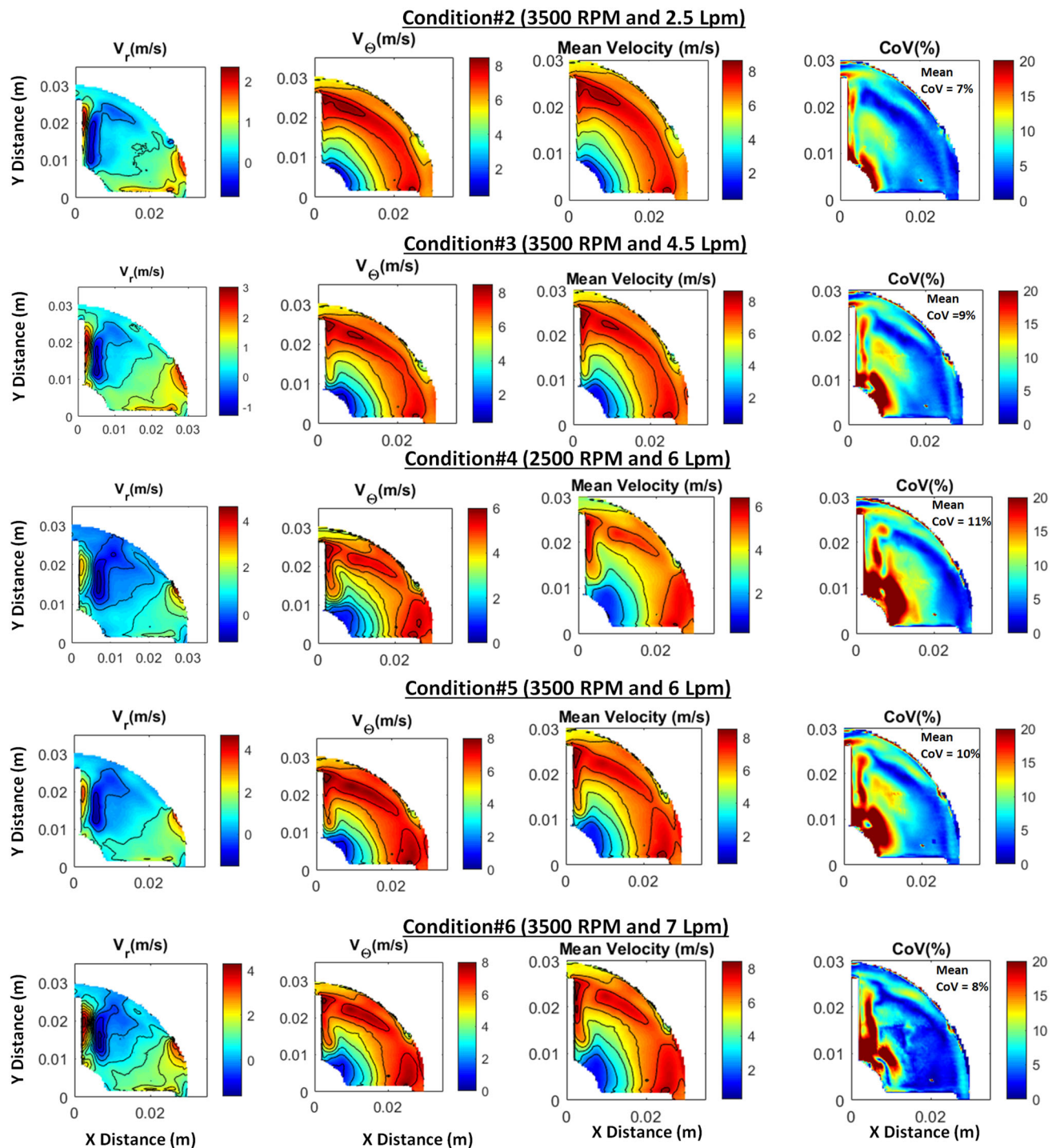


FIGURE 8. Mean velocity contour with coefficient of variation ($\text{CoV} = 100 \times \text{standard deviation}/\text{mean}$) from PIV measurements in three labs in the blade passage region (CS#2). The mean CoV value, spatially averaged over the 2D cross-section, is shown as an insert in the CoV contour.

credibility of the CFD models for complex medical devices. A detailed description on how to evaluate the applicability of validation to the real context of use of the computational model is provided in the ASME V&V 40 standard (Section 8.3),²⁸ and in a detailed

framework specific to applicability analysis for biomedical models.²²

The inter-laboratory study also enabled us to evaluate and understand the applicability of PIV as a validation tool for complicated devices such as cen-

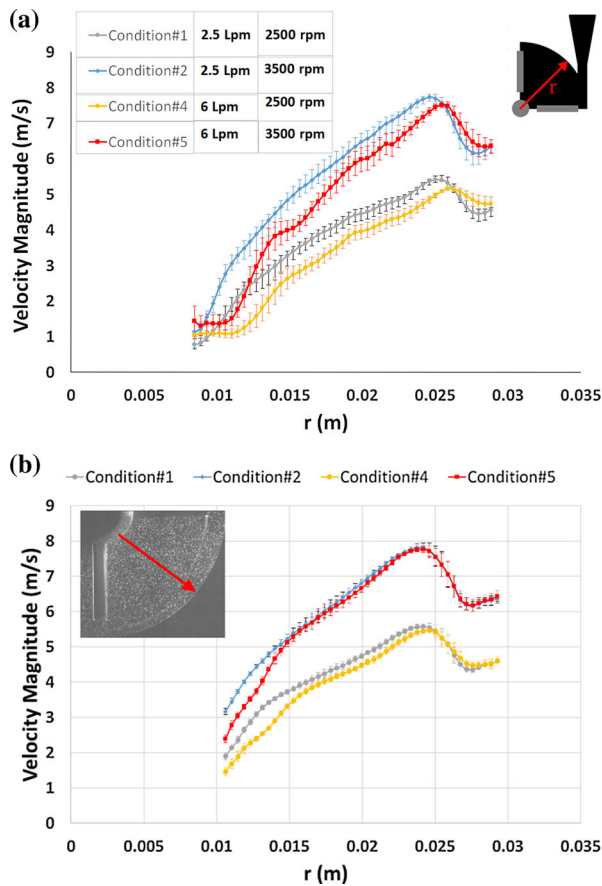


FIGURE 9. (a) Mean velocity magnitudes with standard error ($n = 4$ datasets) along the diagonal line bisecting the first quadrant of the pump (CS#2) at multiple flow conditions (see Table 2). (b) Mean velocity magnitudes with standard error ($n = 4$ datasets) along the diagonal line bisecting the second quadrant of the blade passage region (CS#3) at multiple flow conditions.

trifugal blood pumps. Our results showed good agreement among laboratories for velocity measurements in most measurement locations. Overall inter-laboratory variability in velocity measurements, measured as mean percent coefficient of variation, was approximately $\sim 10\%$ or less for most planes (Fig. 8). The intra-laboratory variability was slightly lower but still comparable to CoVs obtained from inter-laboratory data inside the pump in the blade passage and the back-gap regions. Raw PIV images (e.g., Fig. 4) showed that the particle images at most of the locations were clear with minimal image distortion and a good signal to noise ratio. Optical clarity was achieved by: building major components of the pump, including the housing, rotor, and the blades, using acrylic; using a blood-analog fluid with index of refraction matching that of the acrylic; and using fluorescent particles and a camera lens filter (by 2 of the 3 labs) to minimize the imaging artifacts due to light scattering and reflection. In addition, by applying the best practices for PIV

image capturing and post-processing¹⁰ to select particle image size, time delay between light pulses, interrogation window size, and the number of particles per interrogation window, we were able to further minimize the experimental uncertainties in the PIV measurements.

Despite following a standard protocol for PIV measurements, both intra- and inter-laboratory variabilities were more than 20% in some locations. The variabilities were greatest near the vertical blade edges and in the regions surrounding the stainless steel hub (e.g., Fig. 8). Raw PIV images (e.g., Fig. 4a) indicated that the laser light reflecting off of the blade edges and the stainless-steel hub reduced the signal-to-noise ratio and increased the uncertainty in the velocity measurements. Conversely, the intra- and inter-laboratory variabilities near the horizontal blades was below 20% (e.g., Fig. 8) since the light reflection was not an issue in this direction (e.g., Fig. 4a). Using multiple test laboratories also allowed the identification of potential experimental issues; for instance, the RMS velocity for Lab-2 was 2–3 times greater than the other two laboratories (Fig. 7b). One reason for the larger velocity fluctuations was the use of non-fluorescent particles by Lab-2 which prevented them from increasing the image signal-to-noise ratio by filtering the reflected laser light. However, the mean velocities measured by Lab-2 were still within $\sim 10\%$ of the other laboratories suggesting that the mean velocity data was not influenced significantly by the large RMS values for Lab-2.

The inter-laboratory variability was also high (35% for condition #2) in the pump exit diffuser region. In comparison, the corresponding intra-laboratory variability was only 17%. The quality of the PIV images was acceptable in this region (e.g., Fig. 4d) and did not likely contribute to the high variability. The variability in this location instead stems from inherent differences in the flow patterns of the exit jet (Fig. 13). While the direction of jet asymmetry was reproducible across laboratories, the shape of the flow profile differed among the laboratories. For example, Fig. 13 shows that exit jets from all three laboratories were tilted towards the inner diffuser wall at pump flow condition #2. However, the tilt was more pronounced for Lab-2 compared to the other two laboratories, thereby causing a significant increase in inter-laboratory variability. Reasons for this discrepancy may be related to periodic turbulent/transitional flow, flow separation, large-scale unsteadiness, and swirl observed in the experiments in this region that made it especially sensitive to flow conditions and experimental setup. For the 2.5 L/min scenario, the Reynolds number with reference to the throat region (4.39 mm in diameter) upstream of the diffuser is ~ 3600 , while the Reynolds number a short distance downstream is only ~ 2200

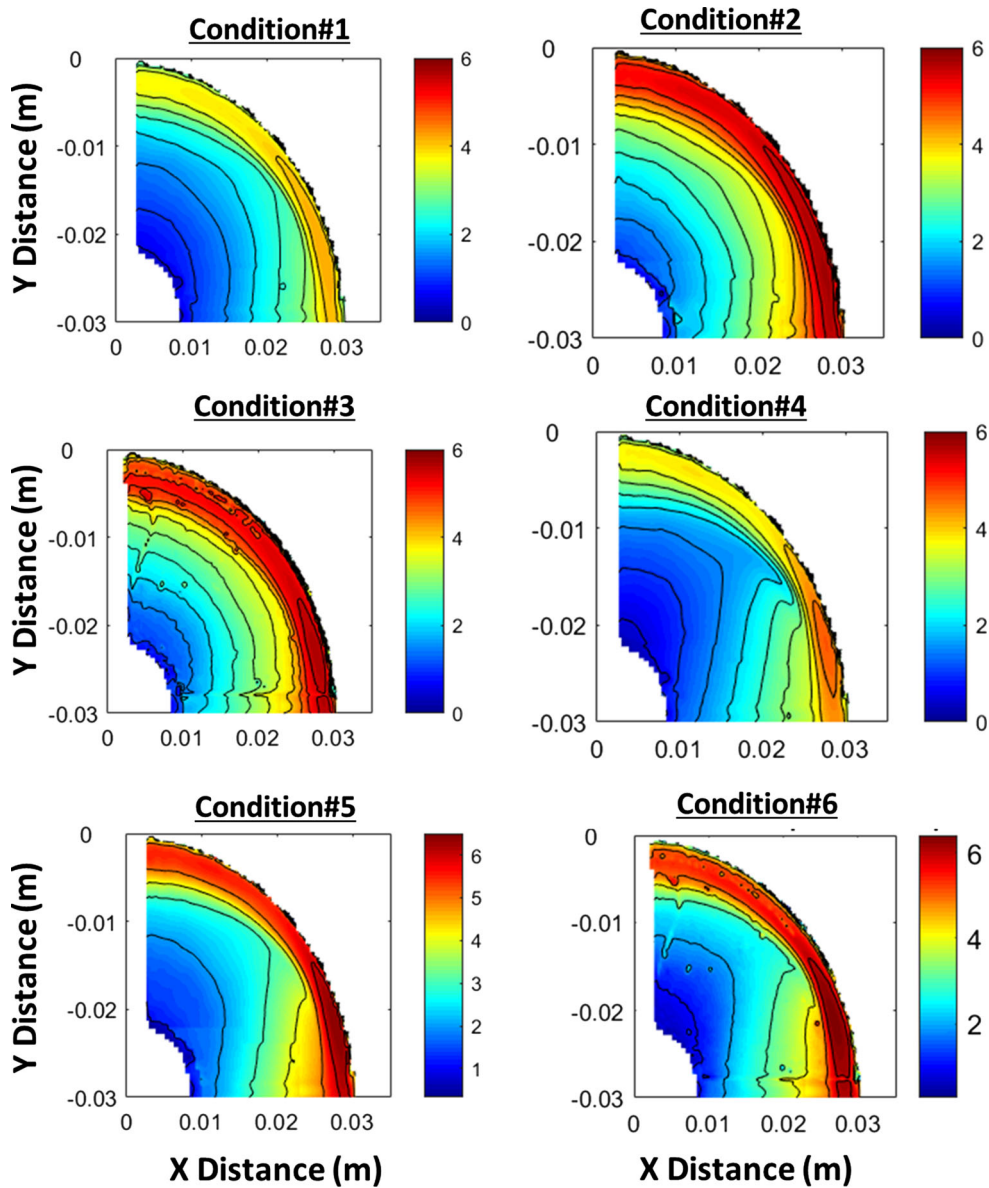


FIGURE 10. Velocity contours in the 1 mm back-gap region beneath the rotor in quadrant #1 (CS #4). PIV images for one of the four datasets had laser light scattering artifacts and hence was not considered for estimating the mean velocities.

(Location 2 in Fig. 13 where $d \sim 7$ mm). The throat diameter, diffuser dimensions, and the Reynolds number for this condition are similar to the geometry and flow conditions examined in the FDA nozzle model, where the results also showed similar inter-laboratory variabilities in the velocity profiles in the nozzle diffuser region.²⁵ The lab-to-lab variability in viscosity, density, and flow rate introduced a $\sim 10\%$ uncertainty in Reynolds number that was enough to cause variations in the exit jet for the nozzle geometry.¹⁰ Similar effects may have impacted the flow field in the diffuser region of the blood pump geometry. Future studies should investigate the sensitivity of the outlet jet orientation to slight variations in the flow

rate, pump rotational speed, pump geometry, fluid properties, laser sheet positioning, and camera alignment.

Relatedly, because flow separation and regions of relatively low fluid velocity occur in the diffuser, shear rates in some regions of the diffuser will be low and the Newtonian approximation less justified. This limitation should be acknowledged in future use of the provided benchmark data. Indeed, Trias *et al.*,²⁹ studied the influence of non-Newtonian effects on the hemodynamics in the FDA nozzle geometry using computational modeling and found that the Newtonian approximation underpredicts the normalized index of hemolysis (NIH) by nearly 20% compared to

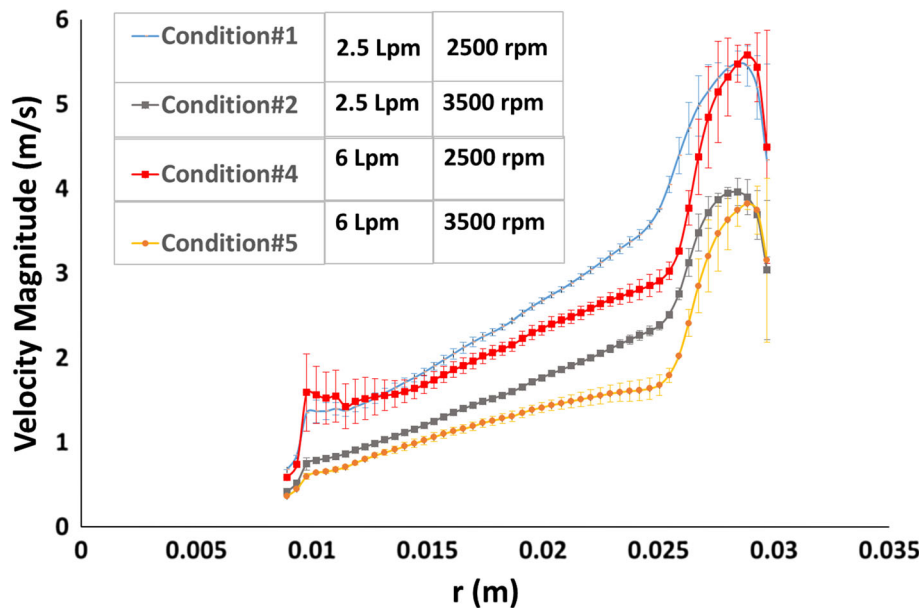


FIGURE 11. Profile of velocity magnitude with the standard error ($n = 3$) along a diagonal line bisecting the first quadrant in the back-gap region (CS#4—see Fig. 4c).

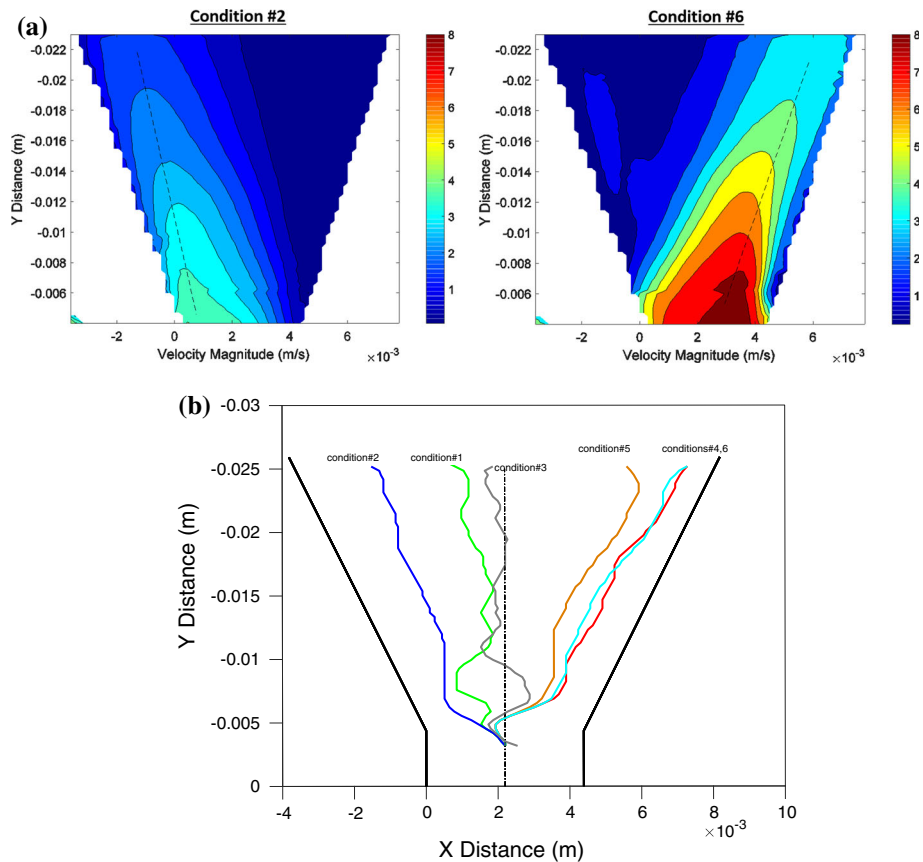


FIGURE 12. (a) Mean velocity contours in the exit diffuser region (CS#5) for conditions #2 and 6. Grey dotted lines represent the approximate center-line of the jet ($n = 4$). (b) Center-line of the exit jet along the length of the diffuser illustrating asymmetry in the exit jet (plotted only for lab 3b). Jet center-lines were extracted by collecting the locations of peak velocity at each Y location along the axis of the diffuser region.

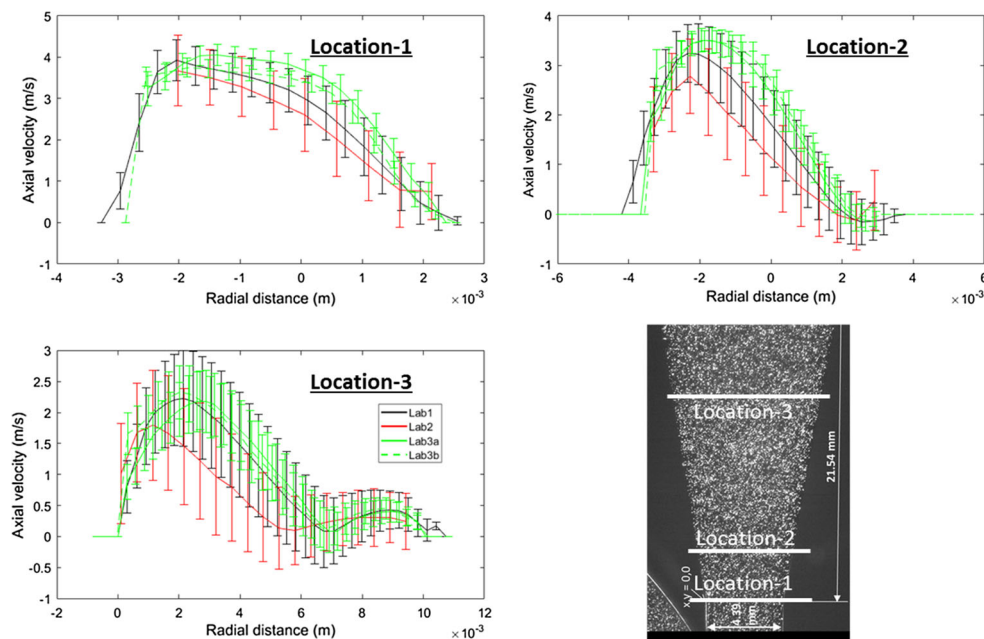


FIGURE 13. Axial velocity profile along three locations (see image inset) in the diffuser region (condition #2). The error bars provide the RMS velocity obtained from 500 image pairs for each laboratory.

non-Newtonian rheology models (Fig. 9 in Trias *et al.*²⁹). Thus, investigating the influence of non-Newtonian hemorheology on the pump hemodynamics is also an important topic of future work.

Besides characterizing the velocity fields, our results also highlighted important flow features in the pump and examined how they are affected by the pump flow rate and the rotational speed. The inlet mean velocity profiles and the turbulent intensities were dependent upon the flow rate (and not the rotational speed) and were different for four of the six flow conditions (Fig. 6 and Table 2). In contrast, the velocity field inside the pump was primarily dependent on the pump rotational speed rather than the flow rate. At the same rotational speed, the velocity magnitudes were similar for all of the flow rates in the blade passage and back-gap regions of the pump (Figs. 8 and 10). However, depending upon the flow rates, subtle differences in the velocity profiles were noticeable in these locations (Figs. 9 and 11). Specifically, as the flow rate increased, the flow was distributed more radially outward, with the location of peak velocity shifting by up to ~ 1 mm (Fig. 9). In addition, the increase in flow rate also reduced the velocity around the central hub region (Figs. 8, 9, 10, and 11). These subtle variations in the velocity profiles are potentially responsible for triggering large-scale flow differences in the diffuser region. The outward shift in the peak velocity (by ~ 1 mm) in the blade passage region potentially caused the jet to tilt towards the outer diffuser wall for higher flow rates (Fig. 12). In comparison, the jet was tilted towards the inner wall for the lower flow rates.

This asymmetry in the exit jet was also responsible for creating large recirculation zones in the diffuser region. Previous studies have observed similar effects with Day *et al.*⁵ pointing out that for flow rates below design point, the stream lines tend to move radially inward as they contact the cutwater, while the opposite effect happens for flow rates above the design point of the pump. CFD simulation models trying to accurately predict the flow field in the pump should be equipped to capture these small-scale differences in the velocities to accurately simulate major flow features such as the jet asymmetry and the recirculation regions in the exit diffuser.

As mentioned in ASME V&V 40 Standard,²⁸ model credibility can be increased by validating the model for prediction of multiple output quantities (Section 8.2.3). Thus, for high-risk contexts of use, such as when CFD is relied upon to provide evidence of safety and effectiveness of centrifugal blood pumps, the underlying CFD models may need to undergo a systematic hierarchical validation that includes multiple fluid dynamic and biologic quantities of interest, such as the velocity, shear stresses, residence times, and blood damage in a device. This article mainly focused on the velocity field analysis of the PIV data at select cross-sections. Our future reports will also provide inter-laboratory validation data for other important quantities, including viscous and Reynolds shear stress and hemolysis of animal blood. While we focused on presenting data at select pump locations in this article, data from additional locations, such as the front-gap between the impeller and the housing and other

quadrants of the pump, will be presented in future studies. The PIV data from these cross-sections will also be made available for download at https://nciph.ub.org/wiki/FDA_CFD/ComputationalRoundRobin2Pump.

Malinauskas *et al.*¹⁵ provided the preliminary comparison between the experimental data and round-robin CFD simulations of the pump fluid dynamics (from 25 groups) for one of the flow conditions. Our future studies will provide a detailed comparison between the experimental data and the round-robin CFD data for all of the flow conditions at various locations in the pump geometry, including at the blade tips and the cutwater region. Through the generation of standards, FDA Guidance Documents, and publicly available experimental benchmark models and data sets, industry, academia, and regulatory bodies will continue to collaboratively develop CFD methodologies to quantify the credibility of simulations, which will ultimately improve the safety and effectiveness evaluations of medical devices.

ACKNOWLEDGMENTS

Our thanks to Dr. Tina Morrison at the FDA/Center for Devices and Radiological Health for review of the manuscript and helpful comments. Matthew Giarra (Rochester Institute of Technology) was the principal design engineer for the blood pump model, under the direction of Dr. Steven W. Day and in collaboration with Dr. Richard A. Malinauskas.

CONFLICT OF INTEREST

All authors declare that they have no conflicts of interest.

ETHICAL APPROVAL

This article does not contain any studies with human participants or animals performed by any of the authors.

REFERENCES

- ¹Aycock, K. I., R. L. Campbell, F. C. Lynch, K. B. Manning, and B. A. Craven. The importance of hemorheology and patient anatomy on the hemodynamics in the inferior vena cava. *Ann. Biomed. Eng.* 44:3568–3582, 2016.
- ²Behbahani, M., M. Behr, M. Hormes, U. Steinseifer, D. Arora, O. Coronado, and M. Pasquali. A review of computational fluid dynamics analysis of blood pumps. *Eur. J. Appl. Math.* 20:363, 2009.
- ³Bhushan, S., D. K. Walters, and G. W. Burgreen. Laminar, turbulent, and transitional simulations in benchmark cases with cardiovascular device features. *Cardiovasc. Eng. Technol.* 4:408–426, 2013.
- ⁴CDRH. CDRH regulatory science report, <http://www.fda.gov/downloads/MedicalDevices/ScienceandResearch/UCM521503.pdf>, 2018.
- ⁵Day, S. W., and J. C. McDaniel. PIV measurements of flow in a centrifugal blood pump: steady flow. *J. Biomech. Eng.* 127:244, 2005.
- ⁶Delorme, Y. T., K. Anupindi, and S. H. Frankel. Large eddy simulation of FDA's idealized medical device. *Cardiovasc. Eng. Technol.* 2013. <https://doi.org/10.1007/s13239-013-0161-7>.
- ⁷Fabritious, B. Application of Genetic Algorithms to Problems in Computational Fluid Dynamics. Exeter: University of Exeter, 2014.
- ⁸Giarra, M. N. Shear Stress Distribution and Hemolysis Measurements in a Centrifugal Blood Pump. Rochester: Mechanical Engineering, Rochester Institute of Technology, 2009.
- ⁹Haddad, T., A. Himes, L. Thompson, T. Irony, R. Nair, and MDIC Computer Modeling and Simulation Working Group Participants. Incorporation of stochastic engineering models as prior information in Bayesian medical device trials. *J. Biopharm. Stat.* 27:1089–1103, 2017.
- ¹⁰Hariharan, P., M. Giarra, V. Reddy, S. W. Day, K. B. Manning, S. Deutsch, S. F. Stewart, M. R. Myers, M. R. Berman, G. W. Burgreen, E. G. Paterson, and R. A. Malinauskas. Multilaboratory particle image velocimetry analysis of the FDA benchmark nozzle model to support validation of computational fluid dynamics simulations. *J. Biomech. Eng.* 133:041002, 2011.
- ¹¹Himes, A. H., T. Haddad, and D. Bardot. Augmenting a clinical study with virtual patient models: Food and Drug Administration and industry collaboration 1. *J. Med. Dev.* 10(3):030947, 2016.
- ¹²Smithee, I., and S. P. Gent. Computational fluid dynamics modeling of blood as a heterogeneous fluid. In: Design of Medical Devices Conference, 2018.
- ¹³Janiga, G. Large eddy simulation of the FDA benchmark nozzle for a Reynolds number of 6500. *Comput. Biol. Med.* 47:113–119, 2014.
- ¹⁴Lance, B. W., J. R. Harris, and B. L. Smith. Experimental validation benchmark data for computational fluid dynamics of mixed convection on a vertical flat plate. *J. Verif. Valid. Uncertain. Quant.* 1:021005, 2016.
- ¹⁵Malinauskas, R. A., P. Hariharan, S. W. Day, L. H. Herbertson, M. Buesen, U. Steinseifer, K. I. Aycock, B. C. Good, S. Deutsch, K. B. Manning, and B. A. Craven. FDA benchmark medical device flow models for CFD validation. *ASAIO J.* 63:150–160, 2017.
- ¹⁶McCroskey, W. J. A Critical Assessment of Wind Tunnel Results for the NACA 0012 Airfoil. Moffett Field: N.A.a.S. Administration, 1987.
- ¹⁷Morrison, T. M., M. L. Dreher, S. Nagaraja, L. M. Angelone, and W. Kainz. The role of computational modeling and simulation in the total product life cycle of peripheral vascular devices. *J. Med. Device* 2017. <https://doi.org/10.1115/1.4035866>.

- ¹⁸Nguyen, T. T. A method for matching the refractive index and kinematic viscosity of a blood analog for flow visualization in hydraulic cardiovascular models. *J. Biomech. Eng.* 126:529, 2004.
- ¹⁹Oberkampf, W. L., and T. G. Trucano. Verification and validation in computational fluid dynamics. *Prog. Aerosp. Sci.* 38:209–272, 2002.
- ²⁰Oberkampf, W. L., and T. G. Trucano. Verification and Validation in Computational Fluid Dynamics. Albuquerque: S.N. Laboratories, 2002.
- ²¹Passerini, T., A. Quaini, U. Villa, A. Veneziani, and S. Canic. Validation of an open source framework for the simulation of blood flow in rigid and deformable vessels. *Int. J. Numer. Methods Biomed. Eng.* 29:1192–1213, 2013.
- ²²Pathmanathan, P., R. A. Gray, V. J. Romero, and T. M. Morrison. Applicability analysis of validation evidence for biomedical computational models. *J. Verif. Valid. Uncertain. Quant.* 2:021005, 2017.
- ²³Sotiropoulos, F. Computational fluid dynamics for medical device design and evaluation: are we there yet? *Cardiovasc. Eng. Technol.* 3:137–138, 2012.
- ²⁴Steinman, D. A., Y. Hoi, P. Fahy, L. Morris, M. T. Walsh, N. Aristokleous, A. S. Anayiotos, Y. Papaharilaou, A. Arzani, S. C. Shadden, P. Berg, G. Janiga, J. Bols, P. Segers, N. W. Bressloff, M. Cibis, F. H. Gijssen, S. Cito, J. Pallares, L. D. Browne, J. A. Costelloe, A. G. Lynch, J. Degroote, J. Vierendeels, W. Fu, A. Qiao, S. Hodis, D. F. Kallmes, H. Kalsi, Q. Long, V. O. Kheifets, E. A. Finol, K. Kono, A. M. Malek, A. Lauric, P. G. Menon, K. Pekkan, M. Esmaily Moghadam, A. L. Marsden, M. Oshima, K. Katagiri, V. Peiffer, Y. Mohamied, S. J. Sherwin, J. Schaller, L. Goubergrits, G. Usera, M. Medina, K. Valen-Sendstad, D. F. Habets, J. Xiang, H. Meng, Y. Yu, G. E. Karniadakis, N. Shaffer, and F. Loth. Variability of computational fluid dynamics solutions for pressure and flow in a giant aneurysm: the ASME 2012 Summer Bioengineering Conference CFD Challenge. *J. Biomech. Eng.* 135(2013):021016, 2012.
- ²⁵Stewart, S. F. C., P. Hariharan, E. G. Paterson, G. W. Burgreen, V. Reddy, S. W. Day, M. Giarra, K. B. Manning, S. Deutsch, M. R. Berman, M. R. Myers, and R. A. Malinauskas. Results of FDA's first interlaboratory computational study of a nozzle with a sudden contraction and conical diffuser. *Cardiovasc. Eng. Technol.* 4:374–391, 2013.
- ²⁶Stewart, S. F. C., E. G. Paterson, G. W. Burgreen, P. Hariharan, M. Giarra, V. Reddy, S. W. Day, K. B. Manning, S. Deutsch, M. R. Berman, M. R. Myers, and R. A. Malinauskas. Assessment of CFD performance in simulations of an idealized medical device: results of FDA's First Computational Interlaboratory Study. *Cardiovasc. Eng. Technol.* 3:139–160, 2012.
- ²⁷Stiehm, M., C. Wüstenhagen, S. Siewert, N. Grabow, and K.-P. Schmitz. Numerical simulation of pulsatile flow through a coronary nozzle model based on FDA's benchmark geometry. *Curr. Direct. Biomed. Eng.* 3(2):775–778, 2017.
- ²⁸American Society of Mechanical Engineers. Draft Standard (Under Development)—Verification and Validation in Computational Modeling of Medical Devices. New York: ASME.
- ²⁹Trias, M., A. Arbona, J. Masso, B. Minano, and C. Bona. FDA's nozzle numerical simulation challenge: non-Newtonian fluid effects and blood damage. *PLoS ONE* 9:e92638, 2014.
- ³⁰U.S. FDA. Guidance for Industry and Food and Drug Administration Staff—Reporting of Computational Modeling Studies in Medical Device Submissions, 2016.
- ³¹Valen-Sendstad, K., M. Piccinelli, and D. A. Steinman. High-resolution computational fluid dynamics detects flow instabilities in the carotid siphon: implications for aneurysm initiation and rupture? *J. Biomech.* 47:3210–3216, 2014.
- ³²Vogel, J. C., and J. K. Eaton. Combined heat transfer and fluid dynamic measurements downstream of a backward-facing step. *J. Heat Transf.* 107:922, 1985.
- ³³White, A. T., and C. K. Chong. Rotational invariance in the three-dimensional lattice Boltzmann method is dependent on the choice of lattice. *J. Comput. Phys.* 230:6367–6378, 2011.
- ³⁴Zmijanovic, V., S. Mendez, V. Moureau, and F. Nicoud. About the numerical robustness of biomedical benchmark cases: interlaboratory FDA's idealized medical device. *Int. J. Numer. Methods Biomed. Eng.* 2017. <https://doi.org/10.1002/cnm.2789>.